Wavefront-error performance characterization for the James Webb Space Telescope (JWST) Integrated Science Instrument Module (ISIM) science instruments

David L. Aronstein[*a], J. Scott Smith[a], Thomas P. Zielinski[a], Randal Telfer[b],
Severine C. Tournois[c], Dustin B. Moore[d], James R. Fienup[d]

[a]Optics Branch, NASA Goddard Space Flight Center, 8800 Greenbelt Rd., Greenbelt, MD 20771;
[b]Space Telescope Science Institute, 3700 San Martin Dr., Baltimore, MD 21218;
[c]Sigma Space Corporation, 4600 Forbes Blvd, Lanham, MD 20706;
[d]The Institute of Optics, University of Rochester, Rochester, NY 14627

ABSTRACT

The science instruments (SIs) comprising the James Webb Space Telescope (JWST) Integrated Science Instrument Module (ISIM) were tested in three cryogenic-vacuum test campaigns in the NASA Goddard Space Flight Center (GSFC)'s Space Environment Simulator (SES) test chamber.

In this paper, we describe the results of optical wavefront-error performance characterization of the SIs. The wavefront error is determined using image-based wavefront sensing, and the primary data used by this process are focus sweeps, a series of images recorded by the instrument under test in its as-used configuration, in which the focal plane is systematically changed from one image to the next. High-precision determination of the wavefront error also requires several sources of secondary data, including 1) spectrum, apodization, and wavefront-error characterization of the optical ground-support equipment (OGSE) illumination module, called the OTE Simulator (OSIM), 2) f/# and pupil-distortion measurements made using a pseudo-nonredundant mask (PNRM), and 3) pupil geometry predictions as a function of SI and field point, which are complicated because of a tricontagon-shaped outer perimeter and small holes that appear in the exit pupil due to the way that different light sources are injected into the optical path by the OGSE. One set of wavefront-error tests, for the coronagraphic channel of the Near-Infrared Camera (NIRCam) Longwave instruments, was performed using data from transverse translation diversity sweeps instead of focus sweeps, in which a sub-aperture is translated and/or rotated across the exit pupil of the system.

Several optical-performance requirements that were verified during this ISIM-level testing are levied on the *uncertainties* of various wavefront-error-related quantities rather than on the wavefront errors themselves. This paper also describes the methodology, based on Monte Carlo simulations of the wavefront-sensing analysis of focus-sweep data, used to establish the uncertainties of the wavefront-error maps.

Keywords: James Webb Space Telescope, Integrated Science Instrument Module, wavefront sensing, phase retrieval, wavefront-error characterization.

1. INTRODUCTION

The James Webb Space Telescope (JWST) is a large, infrared telescope with a 6.5-meter diameter primary mirror[1]. JWST will be the premier space observatory of the next decade. It is scheduled to launch from French Guiana in October 2018.

The optical train of the observatory consists of the Optical Telescope Element (OTE), followed by the four Science Instruments (SIs), which are housed in a structure called the Integrated Science Instrument Module (ISIM)[2]. The four SIs are the Near Infrared Camera (NIRCam), with a Shortwave (SW) and Longwave (LW) channel; the Near Infrared Spectrograph (NIRSpec); the Mid-

[*] david.aronstein@nasa.gov

Infrared Instrument (MIRI); and the Fine Guidance Sensor (FGS) / Near InfraRed Imager and Slitless Spectrograph (NIRISS). There are redundant instruments on both NIRCam (Module A & B) and FGS (Guider 1 & 2).

Optical ground testing of the JWST is being performed in two stages. The first stage, called *ISIM-Element-level* testing, was a test of the SIs housed in the ISIM only, illuminated using a telescope simulator. This testing was performed during three cryogenic-vacuum test campaigns at NASA's Goddard Space Flight Center (GSFC) in Greenbelt, MD: Cryogenic-Vacuum Test 1 Risk Reduction (CV1RR) occurred from 8/2013 - 11/2013, CV2 was 6/2014 - 10/2014, and CV3 was 10/2015 - 2/2016. The ISIM-Element-level tests are the longest and most complex cryogenic-vacuum test campaigns that have been performed at NASA GSFC. The second stage, called *Optical Telescope Element and Integrated Science* (*OTIS*)-*level* testing, will test the OTE and ISIM together at NASA's Johnson Space Center in Houston, TX. It is scheduled to begin in mid 2017.

The present paper discusses the evaluation of wavefront error for the imaging modes of the JWST SIs, based on data taken during the ISIM Element-level CV2 and CV3 test campaigns.

1.1 ISIM Element-level Cryogenic-Vacuum Testing

The ISIM Element-level cryogenic-vacuum (abbreviated here as cryo-vac or CV) test campaigns were conducted in the NASA GSFC Space Environment Simulator (SES) test chamber. The ISIM structure and the SIs were cooled to the Observatory's on-orbit operational temperature of ~36K, and using a cryo-cooler, MIRI was further cooled to ~6-7K. Limited testing was also performed at an "overdrive temperature" of ~40K, to verify the temperature stability needed by the Observatory, given the range of distances from and orientations with the Sun during operation.

ISIM Element-level requirements on the JWST SIs were verified using test data from the ISIM CV2 and CV3 test campaigns. Our test program was always based on having two distinct campaigns, with the equipment brought to room temperature & pressure in between and run through a vibration test in between. Some improvements and repairs were made to the SIs during the "halftime show" between ISIM CV2 and ISIM CV3; for present purposes, the important changes are:
(1) Detectors / sensor chip assemblies (SCAs) were replaced in NIRCam SW A, NIRSpec, Guider 1, Guider 2, and NIRISS. For all but NIRCam SW A, the detector replacement was planned and was necessitated by degradation issues caused by room-temperature storage in the original Teledyne HgCdTe HAWAII-2RG near-infrared detector arrays[3-4].
(2) Shims were added to the focal plane for Guider 1, Guider 2, and NIRISS.
(3) The microshutter array (MSA) in NIRSpec, the enabling technology in its ability to characterize spatial variations of spectrum, was replaced.

Optical testing of the JWST SIs relied on a key piece of optical ground support equipment (OGSE) called the OTE Simulator (OSIM). OSIM is a 1.8 m (diagonal dimension of a rectangular footprint) spherical-primary telescope that presents beams to the ISIM that mimics the JWST telescope. OSIM is able to steer optical beams to any point of the wide field of view for each SI, it can illuminate each SI with a variety of wavelengths, it can introduce multiple waves of defocus, and it has a series of useful pupil masks and phase plates to test different aspects of ISIM. OSIM was calibrated during a series of three cryogenic-vacuum test campaigns at NASA GSFC.

1.2 ISIM Element-level Requirements & Goals for Wavefront Error Performance Characterization

The wavefront-error performance characterization described in this paper was largely performed in support of verifying requirements that are imposed on the SIs. (All of the performance requirements that the JWST Observatory must meet before launch are verified during SI-level, ISIM Element-level, or OTIS-level testing.) Based on ISIM Element-level test data, the categories of requirements addressed by wavefront-error performance characterization are:

RMS wavefront error: NIRCam SW, NIRISS, and MIRI have requirements on the maximum or average RMS wavefront error introduced by the SIs. For NIRCam SW there are also requirements on the RMS value of the wavefront error partitioned into three spatial-frequency bands. Note that RMS wavefront error requirements for NIRCam LW are verified at SI level, and noise-equivalent angle (NEA) requirements are imposed on Guider 1 & 2 in lieu of RMS wavefront-error requirements.

Wavefront-error 3rd-order aberrations: The last step of the 9-step commissioning procedure for the JWST OTE on orbit is called Multi-Instrument, Multi-Field (MIMF) alignment[5-6]; see **Figure 1**. The purpose of MIMF alignment is to make sure that we are correctly separating system wavefront error between the OTE and NIRCam (the primary wavefront sensor for the Observatory), so that the OTE mirror segments are not aligned so as to imprint the NIRCam wavefront error on the other SIs. The MIMF alignment algorithm needs to know the focus and astigmatism variation over each SI's field of view in order to evaluate the alignment state of the OTE mirrors on orbit.
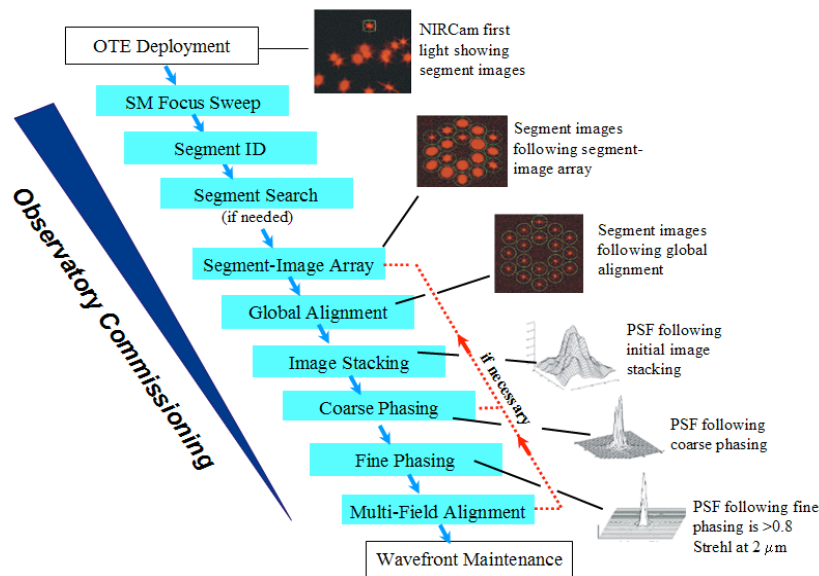

Figure 1: Block diagram of JWST on-orbit commissioning (reprinted from earlier publication[25]).

Focus: We need knowledge of the plane of best focus for a multiple field points in each SI. The ISIM-Element level requirements are actually written in terms of co-focus, knowing the focus of each SI field point relative to a field point in one of the NIRCam SW modules.

Wavefront-error stability: During on-orbit operation, the optical performance of JWST will be re-optimized every 14 days. There are ISIM-Element-level requirements on SI wavefront-error stability during those two-week intervals, evaluated in terms of the stability to the range of temperatures experienced by the SI created by the range of slew maneuvers that are possible during that time interval. There are wavefront-error stability requirements on NIRCam SW, NIRISS, and on the ISIM structure itself.

A goal for wavefront-error performance characterization, but not data taken to address specific ISIM Element-level requirements, is:

Long-term trending of optical "health": The NIRCam instruments contain internal LEDs, mounted out-of-field in the OTE's focal plane, slightly downstream from the instruments' pick-off mirrors (POMs), that can illuminate the Coronagraphic Module (COM) in NIRCam's optical train. Starting during NIRCam module-level testing, the decision was made to take images using these COM LEDs and use them to ascertain the wavefront-error for these optical paths. By taking these measurements at each stage of testing (at NIRCam-level testing, during ISIM CV2 and ISIM CV3, and in the upcoming OTIS-level testing), we have a long-term monitor on the health and stability of the NIRCam optical train, which does not rely on an external light sources or other OGSE (which could vary in alignment or stability from test to test). This test can be thought of as a "canary in the coal mine," a first sign that something noteworthy has changed in NIRCam that requires further investigation.

1.3 Setting SI Internal Focus

With the exception of MIRI, the JWST SIs have internal focus-adjustment mechanisms. Early in each ISIM Element-level cryo-vac test campaign, these mechanisms were adjusted to give optimal performance. There are some noteworthy details to this process:

Each SI team defined "optimal" performance as they wished. The NIRSpec team set their instrument focus using the field point that passes through the small near-square fixed slit in the instrument's internal focal plane. The other SI teams used a weighted averaging scheme of the best focus positions across their field of view.

The FGS Guider 1 & Guider 2 instruments share a common Fine Focus Mechanism (FFM). NIRCam SW A & LW A share one Focus-Adjust Mechanism (FAM), and NIRCam SW B & LW B share another. Unfortunately, the NIRCam SW and LW channels would have wanted opposite directions for a focus adjustment, and the LW channels have to satisfy focus and wavefront-error requirements over their full operating wavelength bandwidth, in the presence of a complicated dependence of focus on wavelength.

Though individual field points, or individual SIs, could be brought into better focus and lower RMS wavefront error, there are no plans for such preferential tunings of the Science Instruments during on-orbit operations. A theme of ISIM Element-level testing is to show that a wide range of performance metrics can be satisfied in all of the JWST SIs simultaneously, without having to reconfigure the observatory to favor certain instruments or parts of the field of view for specific observations.

The wavefront error for each SI's field point tested in the ISIM cryo-vac campaigns was determined using *image-based wavefront sensing*, which in the present document is used interchangeably with *wavefront sensing* or *phase retrieval*. With the exception of the test described in Section 3.2, the ISIM CV tests use *focus-diverse wavefront sensing*, which uses a series of images recorded by the instrument under test in its as-used configuration, in which the focal plane is systematically changed from one image to the next. This set of data, this series of images, is referred to as a *focus sweep*. (In Section 3.2, an alternate method, called Transverse-Translation Diversity wavefront sensing, is used when the standard focus-diverse configuration was not possible.)

These focus sweeps are input into computer algorithms that determine the optical system's exit-pupil wavefront error that is most consistent with all of the measured data. The algorithms simulate light propagation through the optical system, from the exit pupil to the detector. Thus, in addition to the focus-sweep image data, the computer algorithms also need additional information about the optical system and the test setup, including the wavelength spectrum and the pupil illumination (that is, the apodization profile) of the light source, the detailed geometry of the exit pupil (including fold-mirror holes and pupil masks used), the system's f/# at the detector, etc. The sources of this input data will be detailed in Section 2.

Calling the analysis process and algorithms "wavefront sensing" is common but limiting -- in addition to determining the exit-pupil wavefront-error of the instrument under test, the analysis process can often improve our understanding of the pupil illumination[7-9], the f/# at the detector[10-12], and the convolution kernel of the image[13] (which is a combination of the finite size of the source or source-delivery fiber and the jitter environment present when the images were recorded).

There are two general classes of wavefront-sensing algorithms[14], *iterative-transform*[15-18] and *nonlinear optimization (NLO)*[19-21]. Iterative-transform algorithms perform analysis by modeling light propagating back and forth between the exit pupil and image plane of the optical system, imposing constraints from measured data at each location. Nonlinear optimization algorithms only model the light propagating in one direction, from the exit pupil to the image plane, and the knowledge of the optical system is improved by optimizing (minimizing) an error function that compares the modeled and measured detector images.

The original wavefront-sensing algorithm adopted for use for JWST on-orbit commissioning is an iterative-transform algorithm called the Hybrid Diversity Algorithm (HDA)[22-23], and it achieved Technology Readiness Level (TRL)-6[24] in January 2007, based on testing completed on the Testbed Telescope at Ball Aerospace, in Boulder, CO[25]. The ISIM Element-level tests of the JWST SIs involve configurations where the recorded images are sampled below the Nyquist sampling limit, and the technique of Variable Sample Mapping (VSM) was developed to extend the use of the HDA to these undersampled images[26].

There are four independent wavefront-sensing algorithms used by analysts involved in ISIM-Element-level wavefront sensing, two based on iterative-transform and two based on NLO. One is based on the TRL-6 HDA & VSM approach, and the others were compared against the TRL-6

results and other experimental tests and were tested in "blind" studies in which the algorithms were tested on simulated focus-sweep data, independently generated by others on the ISIM Optics team. The wavefront-error answers from the four algorithms were compared carefully, and disagreements beyond the error-budget expectations were analyzed in detail, before the answers were combined into a final, ISIM Element-level prediction for the wavefront error.

The algorithms described above are based on the premise that it is an acceptable approximation to treat all of the diffraction in the optical system under test as occurring in the single propagation from the exit pupil to the detector. That is not valid for the field points tested in NIRSpec that pass through the micro-shutter array (MSA) in the NIRSpec internal focal plane. For these focus sweeps, the ISIM Element-level evaluation of wavefront error is performed with a single algorithm. It models multiple propagation steps between the OSIM light source and the detector and was developed by the co-authors J.S.S. and D.L.A.

1.5 Overview of ISIM Cryo-vac Wavefront-Sensing Tests

The light sources in the OSIM Source Delivery Module (SDM) were chosen to address the needs of the full ISIM cryo-vac test program and to be robust and have high flux output at their operational temperature in the tests. The particular sources used for the ISIM cryo-vac wavefront-error performance characterization tests were chosen for a variety of reasons, including (1) some test wavelengths or SI filters are specified in ISIM Element-level requirements, and (2) to provide continuity with tests performed in SI-level testing or with upcoming OTIS-level testing.

Table 1 provides a summary of the OSIM source properties, SI filters used, average imaging f/#s for the focus sweeps, and the sampling ratio for the image data. The sampling ratio Q is defined as Q = (wavelength) $\times$ (imaging f/#) / (detector pixel size), and images with Q < 1 are said to be undersampled and require a more sophisticated wavefront-sensing algorithm for analysis.

SI	Source Type	Center Light λ (μm)	SI Filter	Average Imaging f/#	Detector Pixel Size (μm)	Sampling Ratio Q
NIRCam SW	Supercontinuum	2.12	F212N	18	18	2.1
NIRCam LW	Tungsten lamp	3.23	F323N	8.8	18	1.6
FGS Guider	LED	2.1		8.1	18	0.9
FGS NIRISS	Laser diode	1.55	F157M	8.7	18	0.7
MIRI	LED w/ narrowband filter	5.6	F560W	7.1	25	1.6
NIRSpec	Laser diode	1.55	F140X	5.4	18	0.5

Table 1: OSIM source properties and image sampling data for the imaging conditions for the wavefront-error performance characterization tests.

2. INPUT DATA FOR WAVEFRONT-ERROR PERFORMANCE CHARACTERIZATION

In this section, we give examples and details of the ISIM CV data recorded and the optical modeling completed that are fed into the wavefront-sensing algorithms.

2.1 Focus sweeps

For each SI field point under test, a focus sweep was recorded by introducing systematic defocus using the OSIM OGSE. OSIM, like the JWST OTE, has an internal focus before the light is relayed to the SIs. The amount of defocus is specified in terms of the distance along the optical axis that the plane of focus is moved at this internal focus. OSIM can introduce up to ±25 mm defocus at the internal OSIM/OTE focus, which corresponds to approximately ±4 waves (peak to valley) of Zernike defocus in the NIRCam SW exit pupil, when operating at a wavelength of 2.12μm and imaging with f/18. Focus sweeps during ISIM CV2 & CV3 included images taken with ±25 mm, ±20 mm, and ±15 mm defocus, and ±10 mm was added for NIRSpec testing.

Broadly speaking, when other factors are held constant, larger point-spread functions (PSFs) in a focus sweep result in better performance of the wavefront-sensing algorithms. The physical size of a defocused point-spread function (PSF) recorded by a detector is proportional to the wavelength of light and the imaging f/#, and asymptotically proportional to the amount of defocus (either measured as a distance between the current plane of the detector and the plane of optimal focus, or as the aount of Zernike-polynomial defocus aberration that is present in the exit-pupil wavefront-error map). **Figure 2** shows example focus-sweep data taken during the ISIM CV3 test campaign, with all images shown on the same physical scale, where the defocus is induced by moving the OSIM light source along the optical axis and is quantified by the change in the plane of focus from the optimal location of the OSIM focus.
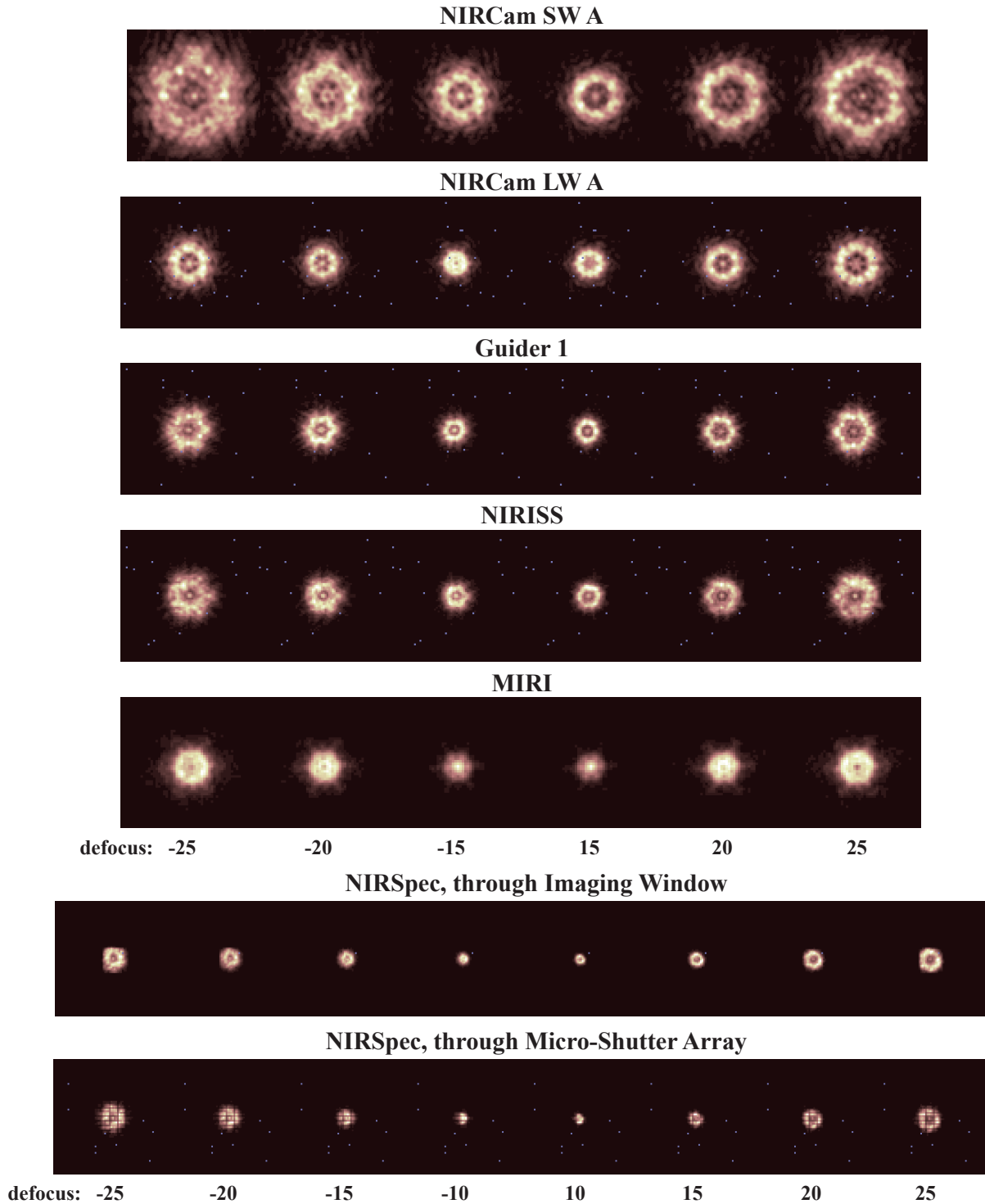
NIRCam SW A

NIRCam LW A

Guider 1

NIRISS

MIRI

defocus: -25   -20   -15   15   20   25

NIRSpec, through Imaging Window

NIRSpec, through Micro-Shutter Array

defocus: -25   -20   -15   -10   10   15   20   25

Figure 2: Example Focus Sweeps for NIRCam SW A, NIRCam LW A, Guider 1, NIRISS, MIRI, and NIRSpec. The light blue dots on the images are "bad" pixels whose data are ignored; pixels could be "bad" intrinsically (e.g., the pixel response could be dead or hot) or due to the specifics of the exposure (e.g., the data in the pixel could be saturated). Defocus is measured in units of mm of displacement from the OSIM focal surface.

Note that we show two example focus sweeps for NIRSpec, that differ in the part of the internal focal plane that the light passes through: One goes through a nearly-square fixed slit, and the other goes through the Micro-Shutter Array (MSA).

Note also that the focus-sweep images for MIRI appear blurrier than the other images. The MIRI detector arrays (Si:As) exhibit an effect called a *detector halo*[27], in which an appreciable portion of the light incident on one pixel gets scattered to neighboring pixels, predominantly along the horizontal and vertical lines of pixels from the original. This effect diminishes rapidly as a function of increased wavelength, but the source in the OSIM Source Delivery Module for testing MIRI operates at 5.6μm, at the low end of the MIRI operating spectral bandwidth. For present purposes, wavefront-error performance characterization for MIRI in the presence of this detector halo just leads to somewhat larger uncertainties.

2.2 OSIM Calibration Data

The OSIM OGSE was calibrated using focus-diverse, image-based wavefront sensing during a series of three cryogenic-vacuum test campaigns at NASA GSFC and it was cross-checked towards the beginning and end of each ISIM CV test campaign using a point-diffraction interferometer. The primary calibration data from wavefront sensing was used in four ways in our wavefront-error performance characterization:

OSIM wavefront-error subtraction: The ultimate goal of our wavefront-error performance characterization is to establish the wavefront error for each SI field point under test. The images shown in **Figure 2**, and the wavefront-error maps determined from them, are reflective of the performance of OSIM and the SI field point in series. In order to isolate the SI field point wavefront error, we must subtract the OSIM wavefront error at this field point from the OSIM + SI wavefront error that is determined from wavefront-sensing analysis on the focus sweep data. We will discuss a subtlety in the OSIM wavefront-error subtraction in Section 2.3, below.

The OSIM wavefront error across its field of view was established using wavefront sensing and cross-checked with results from a point-diffraction interferometer (PDI), at a series of field points. An OSIM source is steered to an arbitrary point in the SI's field of view by adjusting the OSIM's internal pupil stop and fold mirror. Using wavefront-error measurements from select field points and using knowledge of how the light footprint changes across the OSIM mirrors as a source is moved in the SI field, a software tool was developed to provide the OSIM wavefront error at an arbitrary field point. The OSIM team has demonstrated that its top-level wavefront-error requirement has been met, that the OSIM wavefront-error map is known at each field point with an uncertainty ≤ 20 nm RMS.

OSIM Source Spectrum: For wavefront sensing, we need to know the light spectrum arriving at the SI detector, which is a joint property of the OSIM source's spectrum and the transmission spectrum of the SI internal filters (and thin-film coatings on optics, where applicable). The spectrum of the sources used in ISIM Element-level testing were characterized during OSIM cryo-vac testing and cross-checked during ISIM Element-level testing using the spectrographic capabilities in the NIRSpec and NIRISS instruments.

OSIM Source Apodization: For wavefront sensing, we need to know the illumination's apodization (i.e., transverse intensity profile) in the exit pupil of the OSIM + SI field point under test, which is a joint property of the OSIM source's apodization and the intensity transmission profile for the SI field point. The OSIM source apodizations are generally tilted Gaussians in form, though some sources have additional higher-order features and diffractive ringing in their intensity profiles. They were characterized during OSIM cryo-vac testing and the change in the location of the Gaussian shape in the exit pupil and in the tip/tilt terms as a function of the field point under test were evaluated using the same modeling infrastructure that was used to interpolate the OSIM wavefront error to any point in the field.

Pupil Geometry: The OSIM OGSE has a complicated exit-pupil geometry, for two reasons:
1) Focus sweeps were generally performed using an OSIM internal pupil consisting of the same 30-sided (tricontagon) perimeter that is created by the hexagonal mirror segments of the OTE, the central obscuration corresponding to the missing central mirror segment in the OTE, and three line obscurations meant to mimic the spiders that hold the JWST secondary mirror. This part of the pupil will rotate (roll) slightly as a function of the SI field point under test.
2) The pupil also has a series of small obscurations in the main portion of the pupil, caused by the holes in OSIM's Fold Mirror 3 where different light sources are injected into the OGSE. These holes move in the exit pupil substantially as a function of the field point under test.
An example of the OSIM exit pupil is shown in **Figure 3**.
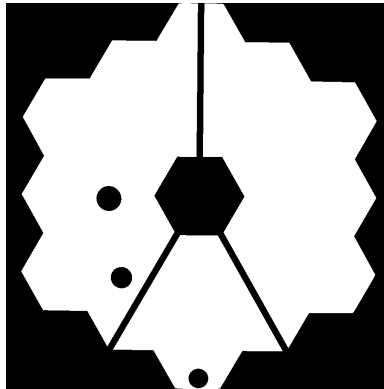
Figure 3: OSIM exit pupil corresponding to illuminating a corner field point in MIRI.

An accurate prediction of the OSIM exit-pupil geometry as a function of the field point under test (specified in terms of the equivalent object angles that would be incident on the OTE) can be made using an optical model of OSIM. A small but important detail is that, since the alignment between OSIM and the SIs can change slightly between ISIM cryo-vac tests and since the OTE will not be in identical alignment to the OSIM, we often prefer to specify field points under test based on where the light lands on the SI SCAs. Our initial mapping between OTE object angles and SI detector locations gets refined and improved during each ISIM cryo-vac test, and we revise our OSIM exit-pupil models each time this mapping is revised.

2.3 f/# and Pupil Distortion Parameters

An initial estimate for the imaging f/# for each SI field point under test comes from an optical model of OSIM + the SI field point.

All of the JWST SIs have some degree of *pupil distortion*, predominantly an anamorphic magnification: ≤ 1% for NIRCam SW, NIRCam LW, and NIRISS, ~2% for MIRI, ~3% for NIRSpec, and ~5% for Guider 1 & Guider 2. This is demonstrated in **Figure 4**, which shows a comparison of the geometry of the OSIM exit pupil and the OSIM + Guider 1 exit pupil at an example field point.
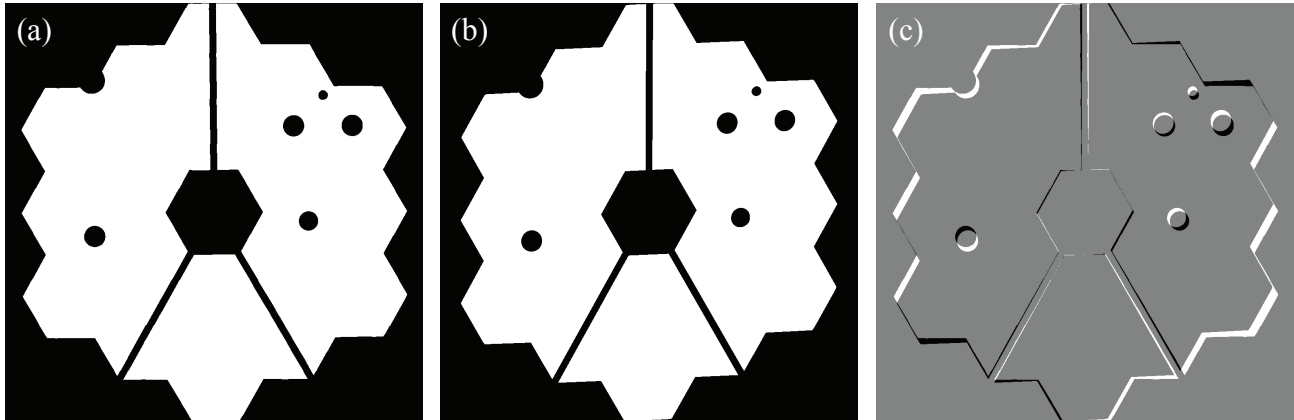
Figure 4: In an example for a field point in Guider 1, (a) the OSIM exit pupil, (b) the OSIM + Guider 1 exit pupil, and (c) the difference between the OSIM + Guider 1 and OSIM exit pupils.

For present purposes, the important issue presented by this pupil distortion is that the calibrated OSIM wavefront-error map cannot simply be subtracted from the OSIM + SI field point wavefront-error map, in order to isolate the wavefront error of the SI alone -- we must do the subtraction in the same "space," either by applying the pupil distortion to the calibrated OSIM map or the inverse pupil distortion on the OSIM + SI field point map established by wavefront sensing. (We choose to do the former.)

For this reason, we require accurate characterization of this pupil distortion. An initial estimate for the pupil-distortion mapping comes from an optical model of OSIM + the SI field point. In order to test both this predicted distortion map, and the predicted imaging f/#, OSIM has a *pseudo-nonredundant mask* (PNRM)[28], a sparse aperture mask whose modulation transfer function (MTF) has little overlap among the spatial-frequency differences between pairs of holes in the mask. **Figure 5** shows the PNRM geometry and a few examples of the MTFs measured using it. (There was a design trade between a fully nonredundant mask and the portion of the exit pupil that is sampled by the mask, and this PNRM design was found to be a better solution for our needs.)
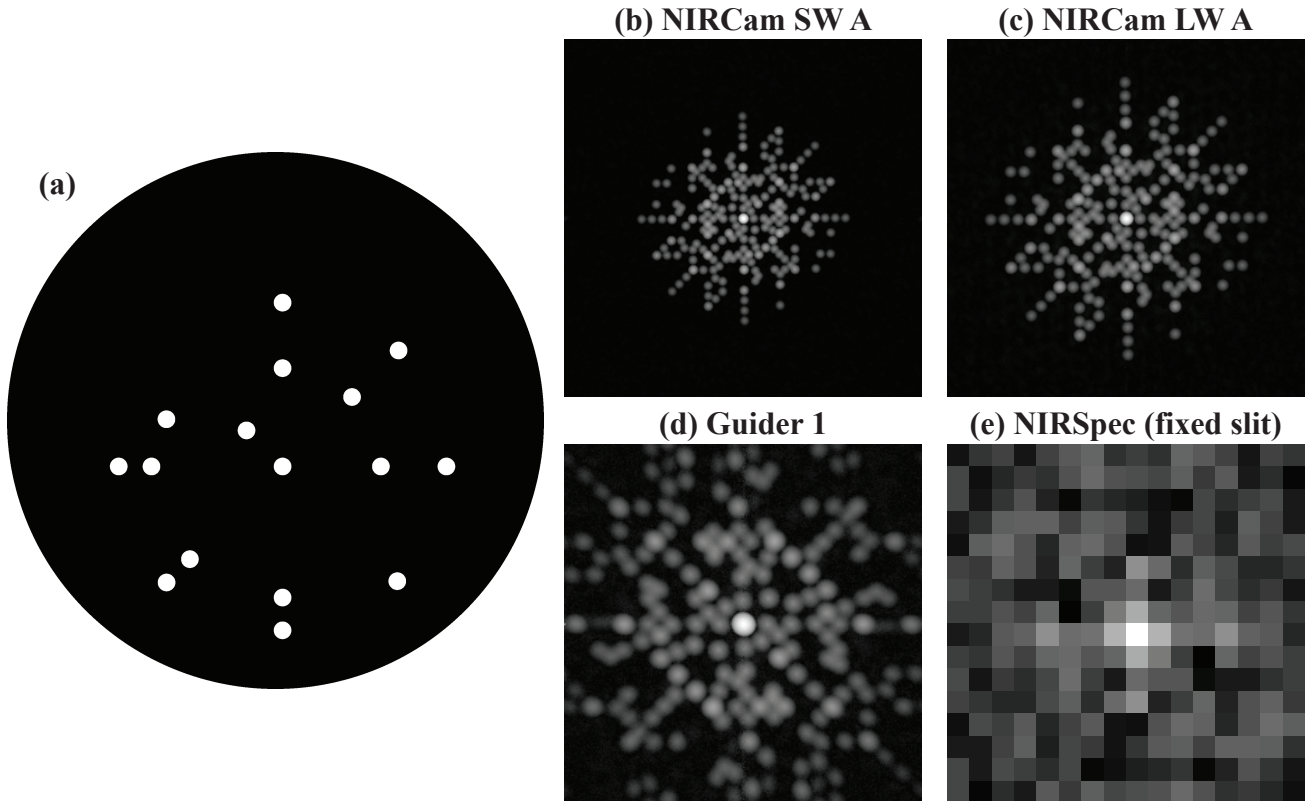
Figure 5: (a) The OSIM Pseudo-Nonredundant Mask (PNRM). Sample modulation transfer functions (MTFs) through the PNRM for (b) NIRCam SW A, (c) NIRCam LW A, (d) Guider 1, and (e) NIRSpec (through the fixed slit). The higher the sampling ratio Q at the detector, the smaller the active area of the MTF.

We took measurements using the OSIM PNRM during ISIM CV testing, as a function of OSIM diversity defocus, for field points in each SI. We used these results to bootstrap the predictions of f/# and pupil distortion mapping from optical modeling. In the end, it turns out that the original optical-modeling results would have been sufficient for input into the wavefront-sensing algorithms, but we had no way to know that *a priori*.

3. SI WAVEFRONT-ERROR PERFORMANCE CHARACTERIZATION

For each SI field point of interest, the data described in Section 2 is input into the ISIM Element team's wavefront-sensing algorithms. As discussed previously, the primary end product sought from this analysis is an evaluation of the SI field point's wavefront-error map, but the algorithm also provides improved knowledge of the exit-pupil apodization, the f/# at the detector, and the convolution kernel of the image (a combination of the finite size of the source or source-delivery fiber and the jitter environment present when the images were recorded). The ISIM Element-level requirements we seek to verify from these tests all connect back to information from only the wavefront-error maps, so we will focus our discussion on those results.

Figure 6 shows an example output wavefront-error map, limited to the low spatial frequency portion (defined here as 0 to 5 cycles per aperture), for the field point in NIRCam SW A for which the focus

sweeps were shown in **Figure 2**. The peak-to-valley extent of this wavefront-error map is 110 nm and the standard deviation is 24 nm RMS.
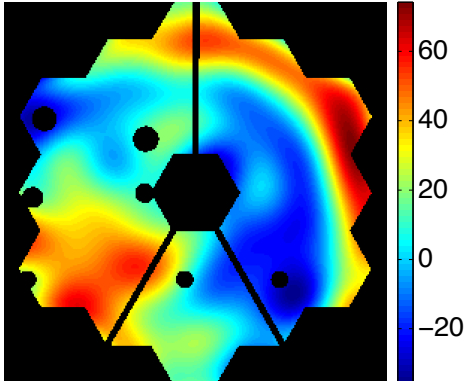
Figure 6: Example low-spatial-frequency wavefront-error map from NIRCam SW A.

In order to deal with issues of data volume and visualization, in Section 3.1 we just show the RMS value of the low spatial frequency wavefront across each SI's field of view, that is found by combining the results from analyzing all of the individual focus sweeps.

3.1 RMS Wavefront Error Across the SI Field of View

The central results of this paper are the RMS wavefront error across the SI field of view, shown below. As introduced in Section 1.3, these RMS wavefront-error values include the impact of the internal SI focus-mechanism settings that were chosen for ISIM CV3; specifically, the RMS wavefront-error values do include the defocus present at each field-point location.
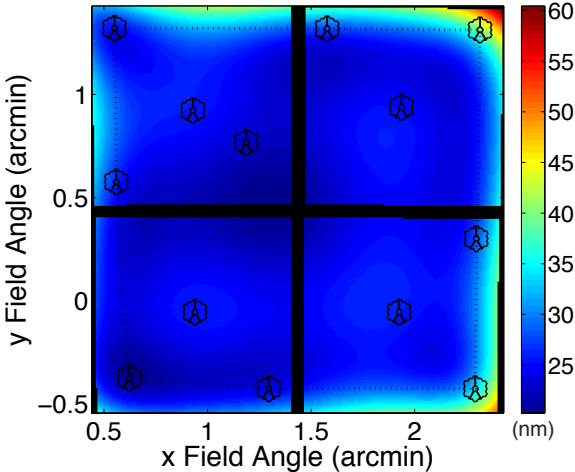
Figure 7: NIRCam SW A RMS wavefront error across the field of view: 21-32 nm RMS on measured field points, 20-39 nm RMS interpolated, and 20-60 nm RMS on the full field of view.
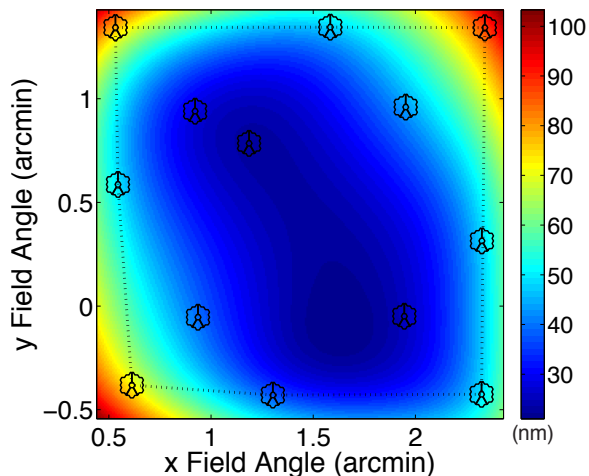
Figure 8: NIRCam LW A RMS wavefront error across the field of view: 24-90 nm RMS on measured field points, 21-90 nm RMS interpolated, and 21-103 nm RMS on the full field of view.
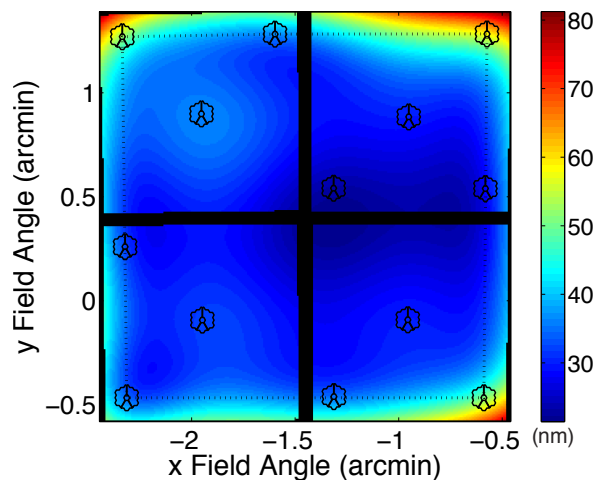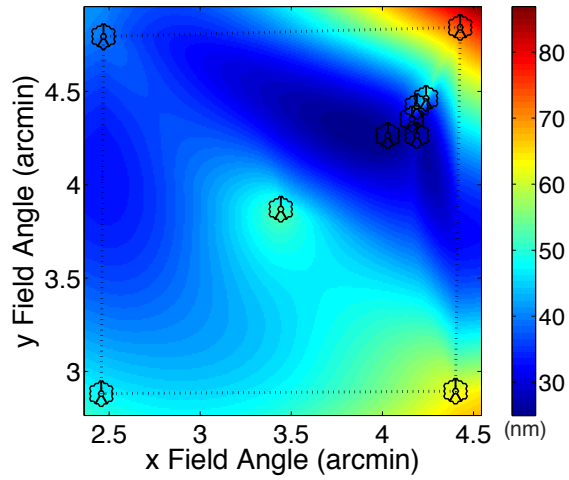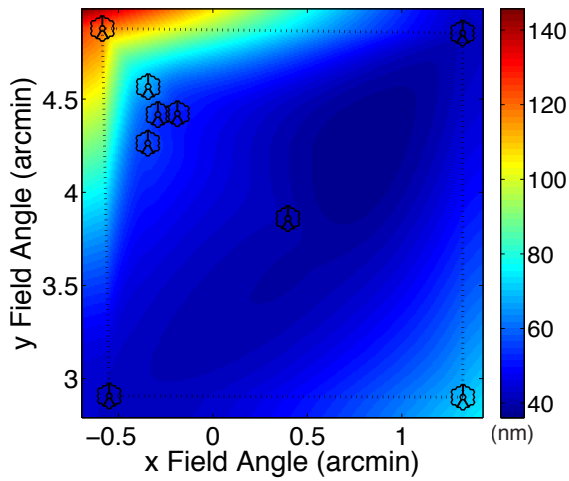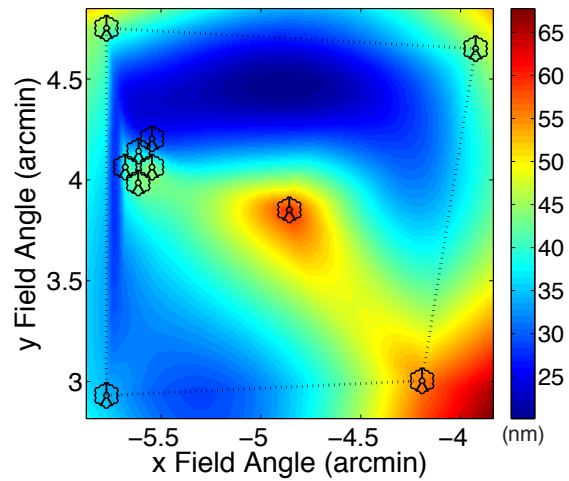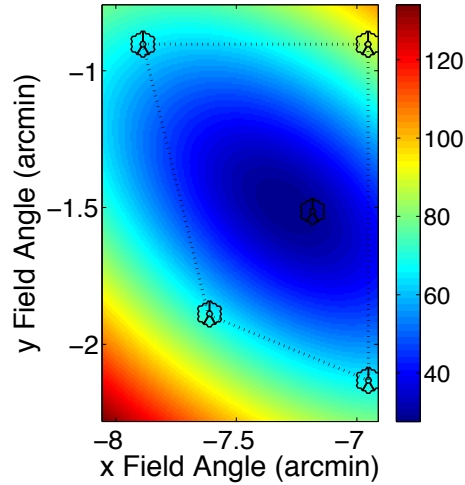

Figure 9: NIRCam SW B RMS wavefront error across the field of view: 26-59 nm RMS on measured field points, 21-59 nm RMS interpolated, and 21-79 nm RMS on the full field of view.
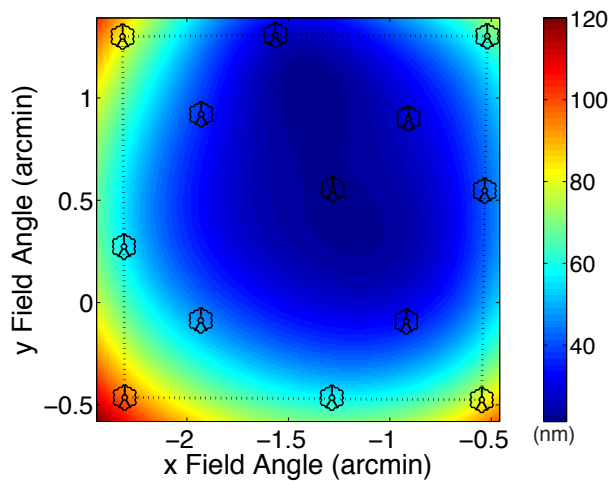
Figure 10: NIRCam LW B RMS wavefront error across the field of view: 24-101 nm RMS on measured field points, 21-101 nm RMS interpolated, and 21-120 nm RMS on the full field of view.

Figure 11: FGS Guider 1 RMS wavefront error across the field of view: 29-74 nm RMS on measured field points, 25-74 nm RMS interpolated, and 25-87 nm RMS on the full field of view.
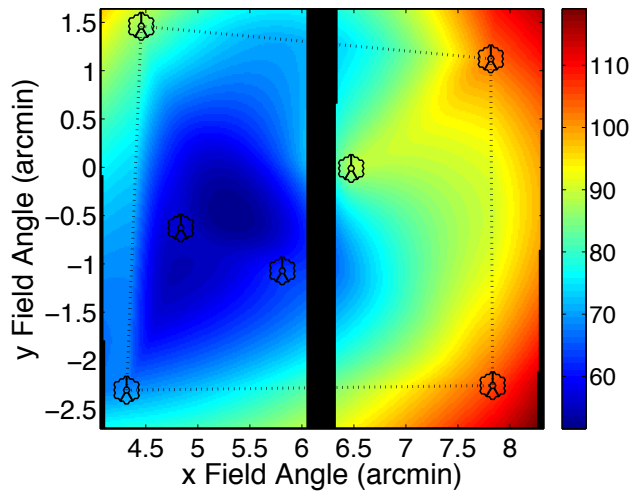

Figure 12: FGS Guider 2 RMS wavefront error across the field of view: 40-119 nm RMS on measured field points, 36-119 nm RMS interpolated, and 36-146 nm RMS on the full field of view.

Figure 13: FGS NIRISS RMS wavefront error across the field of view: 29-60 nm RMS on measured field points, 20-60 nm RMS interpolated, and 20-68 nm RMS on the full field of view.

Figure 14: MIRI RMS wavefront error across the field of view: 45-86 nm RMS on measured field points, 28-87 nm RMS interpolated, and 28-134 nm RMS on the full field of view.

Figure 15: NIRSpec RMS wavefront error across the field of view: 58-109 nm RMS on measured field points, 52-109 nm RMS interpolated, and 52-119 nm RMS on the full field of view.

3.2 NIRCam Coronagraphic Module Wavefront-Error Trending

As introduced in Section 1.2, the NIRCam instruments contain internal LEDs, mounted out-of-field in the OTE's focal plane, that can illuminate the Coronagraphic Module (COM) in NIRCam's optical train. These LEDs are used to take image-based data to establish the wavefront error in this channel, which is then used for long-term trending of NIRCam's optical performance and stability.

Since these LEDs are out-of-field, this method relies on a prism in the NIRCam pupil wheel to deflect the light so that images are formed on the NIRCam SCAs. At the request of the ISIM Optics team, one of the slots in the NIRCam pupil wheel houses an "internal phase-retrieval" (IPR) mask,

consisting of a prism and an undersized circular aperture. (The aperture is undersized to block out some substantial vignetting that occurs because of the out-of-field illumination.)

The NIRCam optical train consists of four stages: the focus and alignment mechanism (FAM), the collimator optics, the pupil& filter wheels, and the camera optics. NIRCam has a low wavefront error across its imaging field of view because the coma and astigmatism in the collimator optics is corrected by largely-equal-but-opposite-sign aberrations in the camera optics. Because the COM optical train starts outside of the NIRCam imaging field of view and because its light path is abruptly redirected by a prism in the pupil wheel, this aberration correction does not occur in the same way for the COM. For this reason, the wavefront-error maps shown below, for the NIRCam SW and LW COM channels, have a much larger RMS wavefront error than what is found in the imaging field of view. Our interest in the COM channel wavefront error is its stability over time; the larger RMS wavefront error is consistent with expectations from optical modeling and is in no way a concern about the performance of the imaging field of view.

Because the COM LEDs are internal to NIRCam, we are severely limited in our ability to take a series of defocused images. For the NIRCam SW tests, we can take images that are in focus or that pass through the +4 wave weak lens in the NIRCam filter wheel. For the NIRCam LW tests, we can only use in-focus images. For these reasons, the pinhole apertures on the LED packages were moved along the optical axis, so that they are no longer strictly conjugate with the detector plane; this shift provides about a half wave of defocus at 3.23μm, for the nominally "in focus" images recorded.

The NIRCam SW COM/IPR trending tests went exceptionally well; example data and results are shown in **Figure 16**. The wavefront-error maps obtained in ISIM CV2 & CV3 agreed to 6.7 nm RMS for module A and 3.9 nm RMS for module B. (The larger discrepancy for module A is due to a piece of particulate in the light path in CV2 that was absent in CV3.) Not only do these results show extreme stability between cryogenic-vacuum tests (and thus before and after vibration & acoustics tests), but the NIRCam COM wavefront error is also sensitive to the rotational alignment of the pupil wheel, and so these results also show excellent pupil-wheel positioning repeatability.

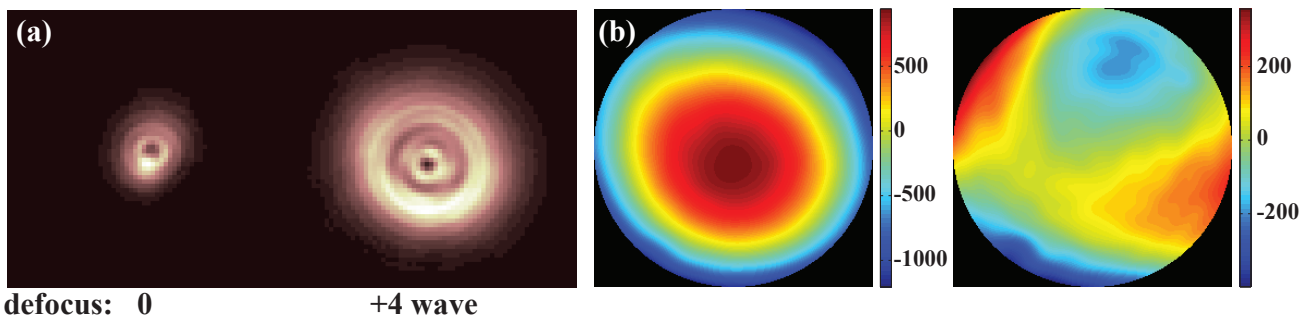defocus: 0   +4 wave

Figure 16: (a) Sample focus sweep for the COM channel and IPR mask in NIRCam SW A. (b) Corresponding wavefront-error maps, showing the wavefront is 557 nm RMS including defocus and 124 nm RMS with defocus removed. As noted above, the larger RMS wavefront error seen in the COM channel is expected from optical modeling and is not a concern for the performance of the NIRCam imaging field of view.

The prisms in the IPR masks for NIRCam LW were installed incorrectly (rotated 90° from the design). There are analogous prisms paired with the actual coronagraphic Lyot masks in NIRCam, so it is possible to use these masks for wavefront-error trending; the downside is that these masks pass light over < 20% of the full aperture, and combined with the lack of large defocus in the NIRCam LW COM channels, this method would not have been a very sensitive "canary in the coal mine" for changes in the NIRCam LW COM light paths over time.   The prospects for long-term trending of the NIRCam LW COM channels were salvaged by the use of Transverse Translation Diversity (TTD) wavefront sensing, a method developed by the research group of Prof. James R. Fienup at the University of Rochester's Institute of Optics[29-31]. TTD is a variation on the phase retrieval technique known as ptychography[33] and the initial simulation applying TTD to NIRCam appeared in an earlier proceeding[34].

Rather than collecting a focus sweep, with the plane of focus systematically varied between successive images, in TTD, images are recorded with a subaperture mask in a pupil plane, and that mask is systematically translated in the plane of the pupil between successive images. Unlike previous implementations of TTD, there were several complicating factors in the NIRCam LW channel characterization:

1) The coronagraphic mask is in the NIRCam pupil wheel, so it rotates through the full NIRCam aperture instead of a simple, linear translation.
2) The initial rotation of the mask is not well known.
3) The conversion between encoder motor steps and angular rotation in the NIRCam pupil wheel is only known approximately.
4) The bounding aperture of the NIRCam LW COM channels is not precisely known.
5) Rotation of the prism with the pupil wheel and source motion required during ISIM Element level testing using OSIM, introduce phase aberrations linear in pupil coordinates that vary with each PSF.

In combination, these factors make it considerably more difficult to accurately estimate the motion of the mask using only the measured image data[34], so two of us (D.B.M. and J.R.F.) extended the TTD method with a bootstrapping approach[35-36]. This method allows the bounding aperture, the linear phase contributing to each PSF, and details of the movement of the subaperture between images to be determined during wavefront-sensing analysis of the image data.

Figure 17 shows the NIRCam LW "MASKRND" coronagraphic Lyot mask, and the composite pupil and wavefront on that pupil that was constructed using this TTD method.
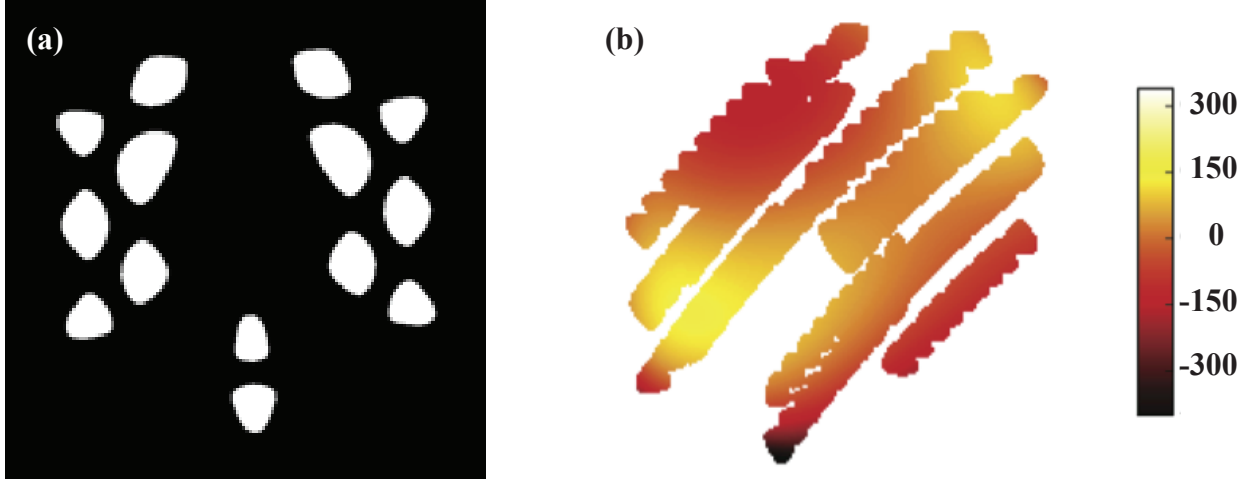
Figure 17: (a) The MASKRND coronagraphic Lyot mask in NIRCam; (b) the wavefront-error map reconstructed using a TTD data set, in which the MASKRND mask is rotated through the NIRCam COM exit pupil.

4. SI WAVEFRONT-ERROR UNCERTAINTIES

The ISIM-Element level requirements on wavefront-error 3rd-order aberrations and on co-focus, described in Section 1.2, are actually requirements on the *uncertainties* of these quantities rather than on the quantities themselves. In short, the 9-step commissioning procedure for the JWST OTE on orbit requires that the input data to the mirror control algorithms have sufficient accuracy to ensure success. In this section, we provide a top-level description of the ways that the main contributors to the error budgets for wavefront-error maps are evaluated.

Uncertainties in the OSIM + SI field point wavefront-error map are evaluated using Monte-Carlo simulations. For each SI, a library of simulated OSIM + SI focus-sweep images are created. The data needed to create these simulated images (the OSIM + SI wavefront-error map, exit-pupil apodization, imaging f/#, OSIM spectrum, finite source size & jitter environment, etc.) and make them look realistic (e.g., detector noise) come from the results of our analysis of ISIM cryo-vac focus-sweep data. The input data provided to the wavefront-sensing algorithms differ from the actual data used to create the simulated images, using our current best knowledge of the uncertainties and distributions of these quantities. We analyze all the focus sweeps in the library for each SI using our wavefront-sensing algorithms, and we perform statistical analysis on the differences between the wavefront-error maps used to create the simulated images and the analysis results of the wavefront-sensing algorithms.

This Monte-Carlo simulation procedure and our results from ISIM CV2 data are presented in detail elsewhere[37], and the uncertainties in the OSIM + SI field point wavefront-error map are summarized in Table . Negligible differences were seen in the uncertainties between iterative-transform and nonlinear-optimization-based wavefront-sensing algorithms. However, the implementation of the VSM/HDA algorithm using graphics processing units (GPUs) is substantially faster than the current implementation of NLO algorithms running on conventional CPU cores.

Science Instrument	Iterative Transform			Nonlinear Optimization			Combined		
	Low	Mid	High	Low	Mid	High	Low	Mid	High
NIRCam SW	3.0	10.7	7.4	3.2	10.1	4.6	2.8	9.7	5.3
NIRCam LW	5.0	14.9	15.6	3.8	13.5	4.8	3.9	13.1	8.6
MIRI	19.3	48.1	7.9	10.2	24.9	6.5	10.1	27.2	6.8
FGS Guider 1	6.2	11.8	7.4	5.1	7.8	1.5	4.8	7.7	3.9
FGS Guider 2	7.3	16.4	17.7	4.9	8.7	1.8	4.9	10.2	9.0
FGS NIRISS	5.3	11.2	7.0	3.8	6.4	1.3	3.4	7.0	3.7
NIRSpec	39.3	13.8	n/a	TBR	TBR	TBR	TBR	TBR	TBR

Table 2: Uncertainties in the recovery of OSIM + SI field point wavefront-error maps, partitioned into three spatial-frequency bands (low, mid, and high), in nm RMS. The uncertainties represent the mean + 2 × standard deviation (i.e., 95% point) of the uncertainties in the Monte-Carlo simulation. The spatial-frequency bands are defined as low = 0-5 cycles in the exit-pupil, mid = 5-30 cycles, and high = 30-100 cycles.

Uncertainties in the OSIM field point wavefront-error map were evaluated by the OSIM team as part of the delivery of OSIM to the ISIM-Element testing team. The top-level wavefront-error requirements for OSIM are that the uncertainty of the full wavefront-error map at any field point must be below 20 nm RMS and the uncertainty of a single, low-order Zernike-polynomial aberration must be below 10 nm RMS. By looking at agreement of wavefront-sensing with PDI results, stability of the OSIM wavefront error across OSIM cryo-vac calibration tests, etc., the OSIM team developed a grassroots error budget for its wavefront-error maps.

Uncertainties due to launch vibration & acoustics were evaluated by evaluating the wavefront-error-map differences between ISIM CV2 and CV3, because the populated ISIM structure underwent vibration & acoustics testing at NASA GSFC between these two test campaigns. As was mentioned in Section 1.1, changes were made to the SIs in between ISIM CV2 and CV3, notably including replacing SCAs for several instruments, and we have no way to separate the changes due to vibration & acoustics and those due to other causes. For that reason, our uncertainties due to launch vibration & acoustics are inherently conservative.

Uncertainties in the 1g to 0g transition and in the SES test chamber to on-orbit thermal profile were evaluated using Structural, Thermal, and OPtical (STOP) modeling. This modeling effort is described elsewhere in this conference[38].

5. CONCLUSIONS

Wavefront sensing during the ISIM cryo-vac test campaigns was highly successful, and we have characterized the focus and wavefront-error maps for each JWST SI at 5 or more field points across its field of view. Trending data of the NIRCam COM channel, using focus diversity for NIRCam SW and transverse-translation diversity (TTD) for NIRCam LW, has also been successful and indicates that the NIRCam optical performance has been extremely stable since integration & testing by the NIRCam team.

The JWST SIs are meeting all requirements that address RMS wavefront error. Requirements on the uncertainties in wavefront-error-related quantities are largely being met, although there are currently

violations in the requirements for the uncertainties of 3rd order aberrations in NIRSpec and for the uncertainties of co-focus in NIRCam. The error budgets that indicate these violations are currently under review. It is low impact if the violations "stand" -- we would have to get requirement waivers and would have to adjust the weighted inputs of the current Multi-Instrument Multi-Field alignment algorithm, in light of these larger-than-expected uncertainties.

At the time of this conference, the ISIM CV3 wavefront-error performance characterization results have not been finalized, but we do not anticipate any noteworthy changes from the results presented here.

6. ACKNOWLEDGEMENTS

REFERENCES

[1] Space Telescope Science Institute, "James Webb Space Telescope: Science Guide," http://www.nasa.gov/pdf/715962main_jwst_science_pub-v1-2.pdf . See also: http://www.jwst.nasa.gov.

[2] Greenhouse, M., "The JWST science instrument payload: Mission context and status," Proc. SPIE 9602, 960202 (2015).

[3] Rauscher, B. J. et al., "Commentary: JWST near-infrared detector degradation -- finding the problem, fixing the problem, and moving forward," AIP Advances 2, 021901 (2012).

[4] Rauscher, B. J., "New and better detectors for the JWST Near-Infrared Spectrograph," Pub. of the Astron. Soc. of the Pacific 126, 942 (2014).

[5] Sabatke, E. et al., "Using multifield measurements to eliminate alignment degeneracies in the JWST testbed telescope," Proc. SPIE 6687, 668707 (2007).

[6] Acton, D. S. and Knight, J. S., "Multi-field alignment of the James Webb Space Telescope," Proc. SPIE 8442, 84423C (2012).

[7] Thurman, S. T., DeRosa, R. T., and Fienup, J. R., "Amplitude metrics for field retrieval with hard-edged and uniformly illuminated apertures," J. Opt. Soc. Am. A 26, 700-709 (2009).

[8] Thurman, S. T. and Fienup, J. R., "Complex pupil retrieval with undersampled data," J. Opt. Soc. Am. A 26, 2503-2511 (2009).

[9] Dean, B. H. et al., "Phase and pupil amplitude recovery for JWST space-optics control," Optical Society of America Frontiers in Optics 2010 conference, paper FWV3 (2010).

[10] Zielinski T. Z. et al., "Determination of the sampling factor in a phase-diverse phase retrieval algorithm," Optical Society of America Frontiers in Optics 2010 conference, paper FWJ3 (2010).

[11] Aronstein, D. L. and Smith, J. S., "Recovery of the image-plane sampling parameter Q within iterative-transform phase retrieval," Optical Society of America Frontiers in Optics 2011 conference, paper FThD6 (2011).

[12] Jurling, A. S. and Fienup, J. R., "Phase retrieval with unknown sampling factors via the two-dimensional chirp z-transform," J. Opt. Soc. Am. A 31, 1904-1911 (2014).

[13] Smith, J. S., "Iterative-transform phase diversity: An object and wavefront recovery algorithm," Optical Society of America Frontiers in Optics 2011 conference, paper FThK2 (2011).

[14] Fienup, J. R., "Phase retrieval algorithms: a comparison," Appl. Opt. 21, 2758-2769 (1982).

[15] Misell, D. L., "A method for the solution of the phase problem in electron microscopy," J Phys. D6, L6-L9 (1973).

[16] Gerchberg, R. W. and Saxton, W. O., "Phase determination from image and diffraction plane pictures in an electron microscope," Optik 34, 275 (1971).

[17] Gerchberg, R. W. and Saxton, W. O., "A practical algorithm for the determination of phase from image and diffraction plane pictures," Optik, 35, 237- 246 (1972).

[18] Saxton, W. O., "Computer techniques for image processing in electron microscopy," Advances in Electronics and Electron Physics, Supplement 10, L. Marton and C. Marton, eds. (Academic Press, New York, NY, 1978).

[19] Fienup, J. R., "Invariant error metrics for image reconstruction," Appl. Opt. 36, 8352 (1997).

[20] Fienup, J. R., "Phase retrieval for undersampled broadband images," J. Opt. Soc. Am. A 16, 1831 (1999).

[21] Thurman, S. T. and Fienup, J. R., "Phase retrieval with signal bias," J. Opt. Soc. Am. A. 26, 1008 (2009).

[22] Dean, B. H., "Hybrid diversity method utilizing adaptive diversity function for recovering unknown aberrations in an optical system," US Patent No. 7,635,832 B2 (12/22/2009).

[23] Dean, B. H. et al., "Phase retrieval algorithm for JWST Flight and Testbed Telescope," Proc. SPIE 6265, 626511 (2006).

[24] Mankins, J. C., "Technology readiness levels: A white paper," NASA, Office of Space Access and Technology, Advanced Concepts Office (1995).

[25] Feinberg, L. et al., "TRL-6 for JWST wavefront sensing and control," Proc. SPIE 6687, 668708 (2007).

[26] Smith, J. S., Aronstein, D. L., Dean, B. H., and Acton, D. S., "Phase retrieval on broadband and under-sampled images for the JWST Testbed Telescope," Proc. SPIE 7436, 74360D (2009).

[27] Rieke, G. H. et al., "The Mid-Infrared Instrument for the James Webb Space Telescope, VII: The MIRI Detectors," Pub. Astro. Soc. Pac. 127, 665 (2015).

[28] Bos, B. J., Ohl, R. G., and Kubalak, D. A., "Pupil alignment considerations for large deployable space telescopes," Proc. SPIE 8131, 81310J (2011).

[29] Guizar-Sicairos, M. and Fienup, J. R., "Image reconstruction by phase retrieval with transverse translation diversity," Proc. SPIE 7076, 70760A1-9 (2008).

[30] Guizar-Sicairos, M. and Fienup, J. R., "Phase retrieval with transverse translation diversity: a nonlinear optimization approach," Opt. Express 16, 7264-78 (2008).

[31] Brady, G. R., Guizar-Sicairos, M. and Fienup, J. R., "Optical wavefront measurement using phase retrieval with transverse translation diversity," Opt. Express 17, 624-639 (2009).

[32] Moore, D. B. and Fienup, J. R., "Subaperture translation estimation accuracy in transverse-translation diversity phase retrieval," Appl. Opt. 55, 2526-2536 (2016).

[33] Faulkner, H. M. L. and Rodenburg, J. M., "Movable aperture lensless transmission microscopy: a novel phase retrieval algorithm," Phys. Rev. Lett. 93, 023903 (2004).

[34] Zielinski, T. P. and Fienup, J. R., "Phase retrieval with a translating Lyot stop coronagraph mask in the JWST," 2009 Signal Recovery and Synthesis (SRS) Topical Meeting of the OSA, paper SWA2 (2009).

[35] Moore, D. B. and Fienup, J. R., "Transverse translation diversity wavefront sensing with limited position and pupil illumination knowledge," Proc SPIE 9143, Space Telescopes and Instrumentation 2014: Optical, Infrared, and Millimeter Wave, 91434F (2014).

[36] Moore, D. B. and Fienup, J. R., "Ptychography for optical metrology with limited translation knowledge," Appl. Opt. 55, 4596-4610 (2016).

[37] Aronstein, D. L. and Smith, J. S., "Phase-retrieval uncertainty estimation and algorithm comparison for the JWST-ISIM test campaign," IEEE Aerospace Conference (2016).

[38] Gracey, R. et al., "Structural, thermal, and optical performance (STOP) modeling and results for the James Webb Space Telescope integrated science instrument module," Proc. SPIE 9904 (2016).